Nanoscale

PAPER

View Article Online
View Journal | View Issue

Cite this: *Nanoscale*, 2022, **14**, 18094

Ru-promoted perovskites as effective redox catalysts for CO_2 splitting and methane partial oxidation in a cyclic redox scheme†

Sherafghan Iftikhar,[a] William Martin,[a] Xijun Wang,[a] Junchen Liu,[a] Yunfei Gao[a,b] and Fanxing Li *[a]

The current study reports $A_xA'_{1-x}B_yB'_{1-y}O_{3-\delta}$ perovskite redox catalysts (RCs) for CO_2-splitting and methane partial oxidation (POx) in a cyclic redox scheme. Strontium (Sr) and iron (Fe) were chosen as A and B site elements with A′ being lanthanum (La), samarium (Sm) or yttrium (Y), and B′ being manganese (Mn) or titanium (Ti) to tailor their equilibrium oxygen partial pressures (P_{O_2}s) for CO_2-splitting and methane partial oxidation. DFT calculations were performed for predictive optimization of the oxide materials whereas experimental investigation confirmed the DFT-predicted redox performance. The redox kinetics of the RCs improved significantly by 1 wt% ruthenium (Ru) impregnation without affecting their redox thermodynamics. Ru-impregnated $LaFe_{0.375}Mn_{0.625}O_3$ (A = 0, A′ = La, B = Fe, and B′ = Mn) was the most promising RC in terms of its superior redox performance (CH_4/CO_2 conversion >90% and CO selectivity ~95%) at 800 °C. Long-term redox testing over Ru-impregnated $LaFe_{0.375}Mn_{0.625}O_3$ indicated a stable performance during the first 30 cycles followed by an ~25% decrease in the activity during the last 70 cycles. Air treatment was effective to reactivate the redox catalyst. Detailed characterizations revealed the underlying mechanism of the redox catalyst deactivation and reactivation. This study not only validated a DFT-guided mixed oxide design strategy for CO_2 utilization but also provides potentially effective approaches to enhance redox kinetics and long-term redox catalyst performance.

Received 13th August 2022,
Accepted 14th November 2022

DOI: 10.1039/d2nr04437d

rsc.li/nanoscale

1. Introduction

Carbon dioxide (CO_2) levels in the Earth's atmosphere are growing at an alarming rate. Meanwhile, the total anthropogenic CO_2 emissions in 2019 have already surpassed the Paris Accord's 2040 target by a factor of 2.[1] As such, cost-effective CO_2 capture and utilization technologies are highly desirable.[2,3] Converting CO_2 to carbon monoxide (CO) is advantageous for a wide range of applications including the production of esters, alcohols, and acids.[4] However, breaking the C═O bond in CO_2 is highly energy-intensive.[5] Electrochemical and photochemical reductions of CO_2 have been explored but these methods still need significant improvements to address low CO_2 conversion, slow electron transfer rates, low product selectivity, and/or low photon efficiency.[6–9] Thermochemical conversion of CO_2 to CO represents another promising alternative, in which an oxygen carrier, also known as a redox catalyst (RC), is first thermally decomposed. CO is then produced by exposing the (partially) reduced RC to CO_2 whereupon the RC is re-oxidized by abstracting an oxygen atom from the CO_2 molecule.[10–17] A key challenge involved in thermochemical methods is that the decomposition of the RC requires a very high temperature (≥1100 °C),[10,18] which can be lowered to ≤950 °C by introducing reducing agents such as hydrogen (H_2) and methane (CH_4) to facilitate CO_2 splitting in an open-loop hybrid redox process (HRP).[19–24] Using CH_4 is attractive since inherently separated CO and syngas with a H_2/CO ratio of ~2 can be obtained *via* the HRP (Fig. 1). In this two-step process, the lattice oxygen released from the RC (represented as $ABO_{3-\delta 1}$) during CH_4 exposure produces syngas *via* the partial oxidation of CH_4 (POx) as indicated by R1 in Table 1. Subsequently, CO is produced by exposing the (partially) reduced RC ($ABO_{3-\delta 2}$) to CO_2 in the second step (R2), in which the RC is re-oxidized by abstracting an oxygen atom from the CO_2 molecule, thereby completing the redox loop. As such, syngas from the POx step is suitable for the synthesis of methanol and liquid fuels, whereas CO from the splitting step can be used separately as a feedstock for chemical production, without the need for complex syngas conditioning and separation steps.[20,23]

[a]*Department of Chemical and Biomolecular Engineering, North Carolina State University, Raleigh, NC 27695-7905, USA. E-mail: fli5@ncsu.edu*
[b]*Key Laboratory of Coal Gasification and Energy Chemical Engineering of Ministry of Education, Shanghai Engineering Research Center of Coal Gasification, East China University of Science and Technology, Shanghai 200237, PR China*
† Electronic supplementary information (ESI) available. See DOI: https://doi.org/10.1039/d2nr04437d

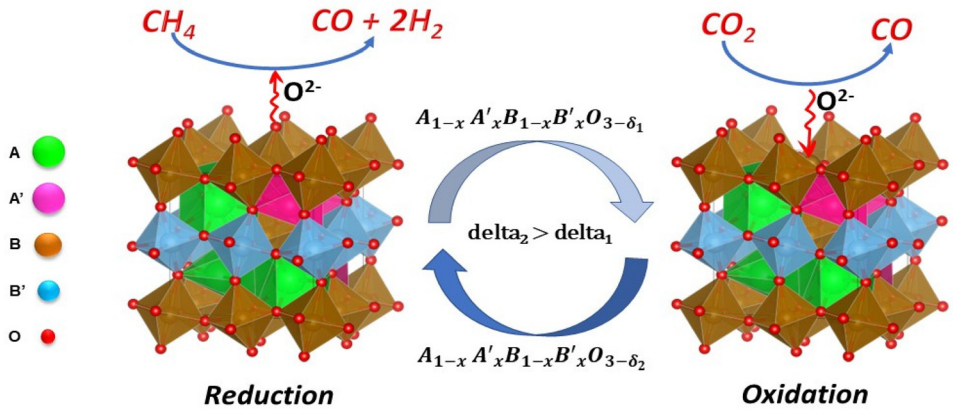

Fig. 1 A simplified schematic of the hybrid redox process.

Table 1 List of key reactions during the methane POx and CO_2-splitting steps (R1 and R2) as well as side reactions in the methane POx step (R3 and R4)

Partial oxidation: R1	$CH_4 + 1/(\delta_2 - \delta_1)ABO_{3-\delta1} \leftrightharpoons 2H_2 + CO + 1/(\delta_2 - \delta_1)ABO_{3-\delta2}$
CO_2 splitting: R2	$CO_2 + 1/(\delta_2 - \delta_1)ABO_{3-\delta2} \leftrightharpoons CO + 1/(\delta_2 - \delta_1)ABO_{3-\delta1}$
H_2 combustion: R3	$2H_2 + 1/(\delta_2 - \delta_1)ABO_{3-\delta1} \leftrightharpoons 2H_2O + 1/(\delta_2 - \delta_1)ABO_{3-\delta2}$
CO combustion: R4	$2CO + 1/(\delta_2 - \delta_1)ABO_{3-\delta1} \leftrightharpoons 2CO_2 + 1/(\delta_2 - \delta_1)ABO_{3-\delta2}$

Iron/iron oxide redox pairs are commonly used as the redox catalyst.[25–33] However, studies have shown that they generally lead to low syngas selectivity and CO_2 conversion.[25,34,35] On the other hand, mixing Fe with other metal oxides has been shown to improve redox properties.[22,24,36–39] For example, it has been reported that CeO_2/Fe_2O_3 [40] and Al_2O_3/Fe_2O_3 [41] mixed oxides favour the partial oxidation of CH_4 to syngas in a chemical looping dry reforming scheme (CLDRS).[42–53] In addition, studies have also shown that promoting Fe-containing materials with other metals such as Ni, Cu, Mn, and Co is an effective approach to acquiring high syngas yields.[54–56] Although tremendous efforts have been made in developing RCs, their optimization still largely relies on heuristics and trial-and-error. Meanwhile, the emergence of mixed oxides has expanded the design space for RCs[28,57–59] thus making it impractical to screen out the promising RCs given the infinitely many possible compositions of mixed oxides. Therefore, effective computational tools are highly desirable to narrow down the design space for RC development and optimization.

The current study investigates the redox performance and long-term stability of perovskite-structured RCs in the context of the HRP. The perovskite materials were chosen due to their unique flexibility in terms of composition, structure and mixed ionic and electronic conductivities.[60] This leads to highly tunable redox thermodynamic and kinetic properties, which are critical for the proposed reactions (R1 and R2).

The size and electronic configurations of the A- and B-site atoms have a great influence on the structure, reducibility, and ionic and electronic conductivities of the mixed oxides.[24,61] Based on the DFT screening, four different perovskite oxides, *i.e.* $Sr_{0.625}La_{0.375}Fe_{0.625}Ti_{0.375}O_{3-\delta}$ (SLFT), $Sr_{0.5}Sm_{0.5}Fe_{0.625}Ti_{0.375}O_{3-\delta}$ (SSFT), $Sr_{0.625}Y_{0.375}Fe_{0.5}Ti_{0.5}O_{3-\delta}$ (SYFT), and $LaFe_{0.375}Mn_{0.625}O_{3-\delta}$ (LFM) were selected. Impregnation with 1 wt% Ru was found to be highly effective in enhancing the redox kinetics for most of these oxide RCs. Ru-LFM, which exhibited the best overall performance, was further characterized and tested for long-term stability. Temperature-programmed reduction/oxidation (TPR/TPO), X-ray diffraction (XRD), transmission electron microscopy (TEM), and X-ray photoelectron spectroscopy (XPS) were performed to determine the phase, stability, redox kinetics, and the deactivation/reactivation mechanisms.

2. Experimental and computational details

2.1. Computational methods

Optimal equilibrium oxygen partial pressures (P_{O_2}s) for the desirable redox catalysts were calculated *via* a Gibbs free energy minimization approach reported previously.[22,55] We have also reported DFT calculations to screen $A_xA'_{1-x}B_yB'_{1-y}O_{3-\delta}$ oxides in the context of chemical looping air separation and CO_2-splitting.[24] Briefly, first-principles simulations were performed at the DFT level implemented by the Vienna *ab initio* simulation package (VASP) with the frozen-core all-electron projector augmented wave (PAW) model and Perdew–Burke–Ernzerhof (PBE) functional. Kinetic energy cut-off was 450 eV with the convergence criteria of 0.01 eV $Å^{-1}$ (force) and 105 eV (energy). Gaussian smearing of 0.1 eV was applied for optimizations. Gamma k-point was used for the $2 \times 2 \times 2$ $A_xA'_{1-x}B_yB'_{1-y}O_{3-\delta}$ perovskite supercells. Each supercell

would contain 8 × (5–δ) or 40–8δ atoms. The GGA + U approach with U_{eff} = 4, 3.9, and 3 was used for Fe, Mn, and Ti. For efficient computation, only FM phase magnetic ordering was applied for all the impregnated structures, given that magnetic ordering has a relatively small influence on oxygen vacancy formation and migration.

2.2. Redox catalyst synthesis

The RCs were synthesized by the modified Pechini method.[62] Nitrate precursors of the metal cations were used for Sr, Sm, Fe, Mn, La, and Y. Titanium butoxide was used as a precursor for Ti. Firstly, the nitrate precursors were mixed in a beaker to the desired stoichiometric ratio with citric acid at a molar ratio to the metal ions of 2.5 : 1. Water was then added, and the resulting solution was stirred using a magnetic stirrer at 300 rpm for 30 minutes at 40 °C. For titanium butoxide, ethanol was added at a 3 : 1 weight ratio to the titanium precursor. This was followed by the addition of ethylene glycol as the chelating agent at a 1.5 : 1 molar ratio to citric acid. This solution was then heated at 80 °C to form a viscous paste, which was then heated overnight at 120 °C. The resulting dried solid was calcined at 900 °C for 10 hours under an oxidative environment. Finally, the desired perovskite was formed and subjected to further characterizations or cyclic testing. 1 wt% of ruthenium (Ru) was also impregnated over the perovskite oxides (SLFT, SSFT, SYFT, and LFM) *via* the wet incipient method. The impregnated sample was then calcined at 900 °C for 10 hours under an oxidative environment.

2.3. Cyclic redox tests

For cyclic redox testing, the calcined perovskites were crushed and sieved to obtain a 250–450 μm range of particles. Approximately 0.4 g of the resulting particles was loaded into a quartz U-tube (4 mm inner diameter), which was placed inside an electric furnace. Connected to the U-tube within the electric furnace were two gas lines. The inlet was configured to have gases introduced from a panel controlled by a computer for automated cyclic valve switching. The outlet contained product gases from the redox cycles which were then delivered to a quadrupole mass spectrometer (Cirrus 2, MKS) for analysis. Samples in the U-tube were pre-treated by exposing them to 30 sccm of H_2 + CO_2 + Ar mixture at 900 °C. The redox performance of the RCs was assessed by exposing the pre-treated samples to 5 redox cycles of CH_4/CO_2 isothermally at 800, 850, 900, and 950 °C, respectively. A fixed flow rate of argon (22.5 sccm) was used throughout the initial temperature ramp to the isothermal temperature (during cyclic redox testing). The redox cycle consisted of a 3 min injection of both CH_4 and CO_2 at 2.5 sccm during the CH_4-POx and CO_2-splitting steps, respectively. Between the two steps, there was a 2-minute argon purge to remove any leftover gases from each step. For long-term testing, 1.5 sccm was used for CH_4 and CO_2.

2.4. Characterization of the redox catalyst

Temperature-programmed reduction/oxidation (TPR/TPO) experiments were performed in a thermogravimetric analyzer (TGA) to study the reduction/oxidation behaviour and CH_4/CO_2 activation. For this type of testing, 10 mg of the sample was loaded into a small crucible within the TGA setup. During the TPR experiments, samples were exposed to 200 sccm of 5 vol% H_2 or CH_4 (balance argon) by simultaneously increasing the temperature from 25 °C to 1000 °C at various heating rates (19, 23, and 27 °C min^{-1}). A similar procedure was used for TPO experiments but with 5 vol% CO_2. Temperature-programmed oxidation of the post-100 cycles RC was also performed in a packed bed by exposing it to 5 vol% oxygen and increasing the temperature from 25 °C to 900 °C at 10 °C min^{-1}. The post-100 cycles RC was also treated in the air for 1 hour at 900 °C for its reactivation. X-ray diffraction (XRD) was performed to identify the phases within the as-prepared and spent forms of the catalysts. The XRD was performed on a Rigaku SmartLab X-ray diffractometer with Cu Kα radiation at 40 kV and 44 mA. The characterization was done *via* a step size method, having a residence time of 2 seconds, and varying the 2θ angle by 0.05° increments from 20° to 80°. High-resolution transmission electron microscopy (TEM) images were also obtained using a field-emission scanning transmission electron microscope (STEM) (JEOL 2010 F) operating at 200 kV. To determine the surface elemental composition of the samples, X-ray photoelectron spectroscopy (XPS) was used. The Kratos Analytical Axis Ultra (monochromatic Al Kα) was operated at 10 mA and 15 kV. The results from XPS were analyzed by CasaXPS software, with an adventitious peak of carbon at 284.8 eV.

3. Results and discussion

3.1. Screening of perovskite oxide redox catalysts

The selection of RC is critical to the HRP since it serves as an oxygen source (POx step) and sink (CO_2-splitting step).[22] From a thermodynamic standpoint, a redox pair ($ABO_{3-\delta1}$/$ABO_{3-\delta2}$) with a high equilibrium partial pressure of oxygen (P_{O_2}) can lead to the over-oxidation of syngas (see R3 and R4 in Table 1) whereas a low P_{O_2}, although favorable for CO_2 splitting, will result in low CH_4 conversions.[22,24] Fig. 2a summarizes the optimal P_{O_2} region for the partial oxidation of methane to syngas and Fig. 2b illustrates the relationship between P_{O_2} and CO_2 conversion at different operating temperatures.

Our previous studies indicate that a P_{O_2} value between 10^{-21} and 10^{-17} atm is optimal for the efficient POx and CO_2-splitting steps within a temperature range of 750 to 900 °C.[22,24] As can be seen from Fig. 2a, the equilibrium P_{O_2} for the Fe/FeO redox pair, a frequently investigated RC, is notably higher than this high performance region. Therefore, fine-tuning the redox properties of the oxide materials is necessary to obtain an optimal P_{O_2}. In a recent study, we performed high-throughput DFT calculations to investigate the oxygen chemical potential of 2401 $A_xA'_{1-x}B_yB'_{1-y}O_{3-\delta}$ perovskites at 950 °C by calculating the Gibbs free energy associated with oxygen uptake/release between discrete oxygen non-stoichiometric levels (δs, see Fig. 2).[24] The dopants considered include Ca, K, Y, Ba, La, and Sm for the A-site and Co, Cu, Mn, Mg, Ni, and Ti for the B-site. The current study focuses on several DFT-predicted compo-

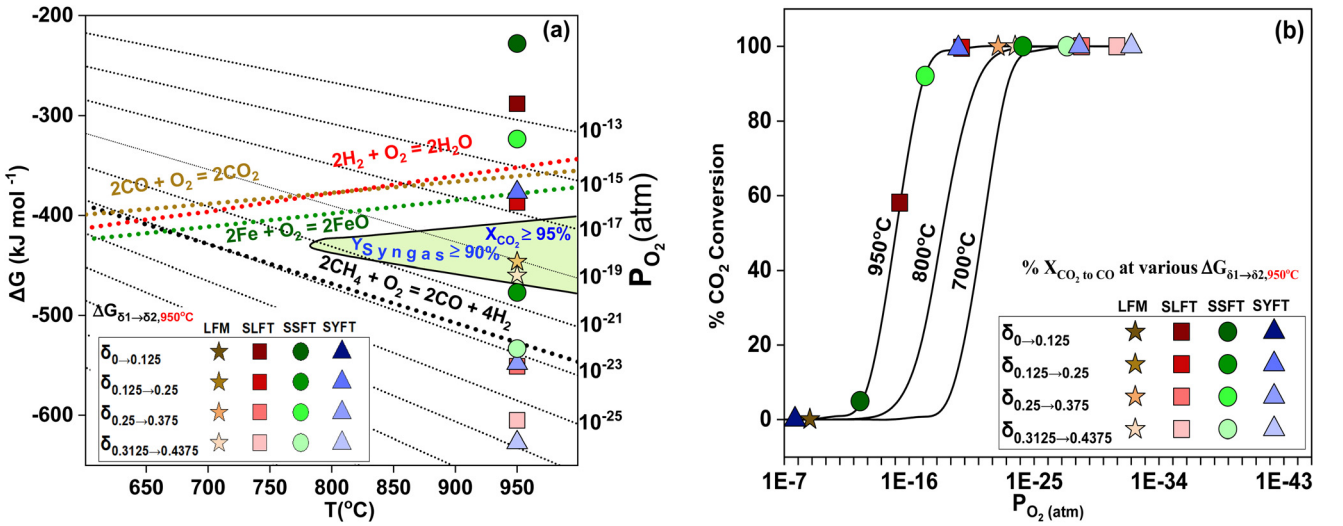

Fig. 2 Thermodynamic analysis of (a) methane POx and (b) CO_2-splitting reactions as a function of P_{O_2} and temperature.

sitions that are suitable for HRP application. The specific compositions include $Sr_{0.625}La_{0.375}Fe_{0.625}Ti_{0.375}O_{3-\delta}$ (SLFT), $Sr_{0.5}Sm_{0.5}Fe_{0.625}Ti_{0.375}O_{3-\delta}$ (SSFT), $Sr_{0.625}Y_{0.375}Fe_{0.5}Ti_{0.5}O_{3-\delta}$ (SYFT), and $LaFe_{0.375}Mn_{0.625}O_{3-\delta}$ (LFM). As shown in Fig. 2a, DFT calculations covered δ ranges with a relatively low resolution due to the limited supercell size for practical calculations. Generally, equilibrium P_{O_2} monotonically decreases with increasing δ. As such, all four materials of interest cover the optimal P_{O_2} region within a viable oxygen non-stoichiometry range for the perovskite oxides, *i.e.*, the discrete data points predicted by DFT cover the entire span of the desirable P_{O_2} region for all four materials. As shown in Fig. 2b, the corresponding P_{O_2} values of the RCs at various δ ranges also favour high CO_2 conversions (see the ESI† for calculation details). The following sections focus on the experimental evaluation and characterization of these redox catalysts.

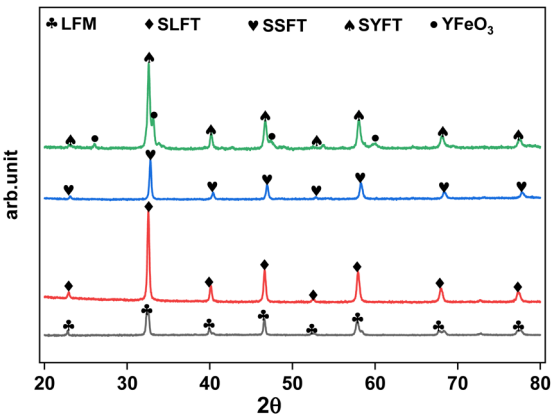

Fig. 3 XRD patterns of the as-synthesized $A_xA'_{1-x}B_yB'_{1-y}O_{3-\delta}$ (PDF for $YFeO_3$: 01-086-8583; PDF for all others: 04-007-9930).

3.2. Phase characterization and redox performance of oxygen carriers

XRD patterns of the as-synthesized $A_xA'_{1-x}B_yB'_{1-y}O_{3-\delta}$ RCs are shown in Fig. 3. An orthorhombus-structured perovskite phase was identified for all the $A_xA'_{1-x}B_yB'_{1-y}O_{3-\delta}$ compositions, expect for SYFT, which contained a $YFeO_3$ phase due to the difficulty in incorporating yttrium into the parent $SrFeO_3$ perovskite structure.[63] The redox performance of the as-synthesized RCs is shown in Fig. 4a. As can be seen, CH_4 conversion varied between 38 and ~97% whereas CO selectivity remained above 80% at 950 °C during the CH_4-POx step. This confirms that the DFT-based materials screening resulted in RCs with suitable P_{O_2} levels for CH_4 partial oxidation without over-oxidizing syngas products. CO_2 conversion also varied between 58 and ~98% at 950 °C. It may be noted, from Fig. 2a, that both CH_4 and CO_2 conversions can be higher than 90% at 950 °C from a thermodynamic standpoint. The lower experimental CH_4 and CO_2 conversions (Fig. 4a) are likely to be due to the slow kinetics of the methane POx step, which can also affect the subsequent CO_2-splitting step. To confirm this, the RCs were impregnated with 1 wt% ruthenium (Ru), which was shown to be active for methane activation.[64–66] The redox performance of Ru-impregnated RCs is shown in Fig. 4c. A significant increase in CH_4 and CO_2 conversions was observed for all the samples. In particular, near 100% CH_4/CO_2 conversions and CO selectivity were observed for Ru-impregnated SSFT and LFM at 950 °C. The effect of Ru was less significant on SLFT, possibly due to the strong metal support interactions. The improvement in the redox performance over Ru-impregnated RCs further confirms that the DFT calculations were effective in predicting the redox thermodynamics of the mixed oxides. Given the improved redox kinetics of Ru-impregnated RCs, we also investigated the redox performance at low temperatures (800–900 °C). The redox performance of the as-synthesized impregnated/non-impregnated RCs at low temperatures is also shown in Fig. 4(a and c). As can be seen, CO selectivity was above 80% in general and above 90% at higher temperatures

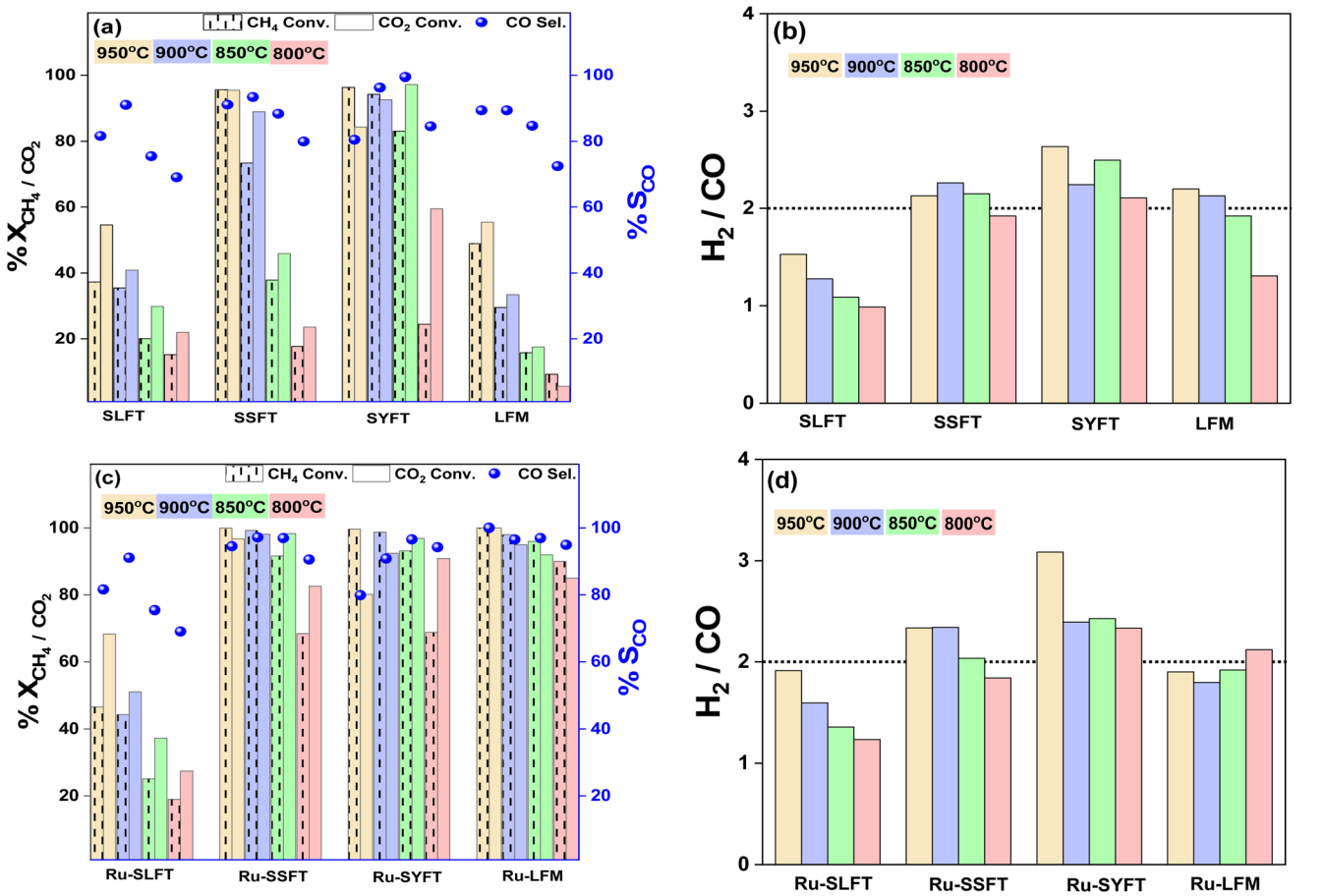

Fig. 4 Redox performance of as-prepared (a) and (b) and Ru-impregnated (c) and (d) $Sr_xA_{1-x}Fe_yB_{1-y}O_{3-\delta}$ at 750, 800, 850, and 900 °C; CH_4 and CO_2 conversions, and CO selectivity (a) and (c), and H_2/CO ratio (b) and (d).

during the CH_4-Pox step. However, relatively low CO selectivity was observed for non-impregnated RCs at 800 °C.

On the other hand, CH_4 and CO_2 conversions varied from 5 to 97% and 20 to ~100% for non-impregnated and impregnated RCs, respectively. Meanwhile, the H_2/CO ratio was near 2 for all the RCs (impregnated and non-impregnated) except at selected conditions for SYFT and SLFT, as shown in Fig. 2(b and d). The H_2/CO ratio was much lower than 2 for SLFT and Ru-SLFT at 800 °C. This may indicate the formation of $SrCO_3$ in the CO_2-splitting step and subsequent "dry reforming" of the carbonate by methane. On the other hand, the H_2/CO ratio for Ru-SYFT varied between 2 and 3, indicating that a fraction of CH_4 was thermally cracked, probably due to the phase segregation indicated in the XRD spectra of SYFT (Fig. 3). Out of all the Ru-doped RCs, Ru-LFM was the most interesting: CH_4 and CO_2 conversions were improved by up to more than 10-fold at 800 °C. Due to its excellent redox performance and coke-resistant nature at 800 °C, Ru-LFM was selected for further investigation and characterization.

3.3. Characterization of 1 wt% Ru-LFM

Temperature-programmed reduction/oxidation experiments were conducted to compare the redox kinetics of impregnated and non-impregnated LFM. The shifts of the DTG peaks to significantly lower temperatures during CH_4-TPR and CO_2-TPO (Fig. 5) confirmed the ease of CH_4/CO_2 activation over Ru-LFM compared to that over LFM. The activation energies (E_a), which

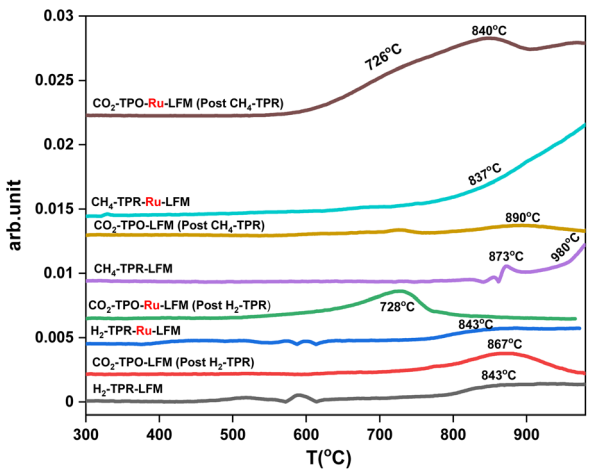

Fig. 5 DTG peaks of Ru-LFM during H_2/CH_4-TPR and CO_2-TPO.

were calculated using the Kissinger method,[67] also decreased from 149 and 201 kJ mol^{-1} to 41 and 78 kJ mol^{-1} for CH_4 POx ad CO_2-splitting, respectively (Fig. S1 and S2 in the ESI†). On the other hand, the activation energies during the H_2 reduction largely remained unchanged for LFM (76 kJ mol^{-1}) and Ru-LFM (83 kJ mol^{-1}). This confirms the role of Ru in accelerating the kinetics for CH_4 and CO_2 conversions and that the redox thermodynamics of the original perovskite would not be affected by Ru impregnation. Meanwhile, XRD patterns of the impregnated and non-impregnated LFM (Fig. S3†) are nearly identical. This confirms that (a) Ru was not incorporated into the original perovskite phase; and (b) the absence of Ru-containing phases further confirmed its high dispersion on the surface. Further XRD analysis of the post-CH_4 and post-CO_2 Ru-LFM samples (Fig. 6) indicated that no additional phases were present. Small shifts in 2θ angles can be observed between the main peaks of the post-CH_4 step sample and post-CO_2 treated sample. This corresponds to the lattice oxygen release and uptake of Ru-LFM, while maintaining its perovskite structure. Under our typical operating conditions, lattice oxygen corresponding to 0.4–0.6 wt% of the sample is reversibly removed in each cycle, although the maximum oxygen capacity corresponds to ~6 wt% of the sample weight (Fig. S4†).

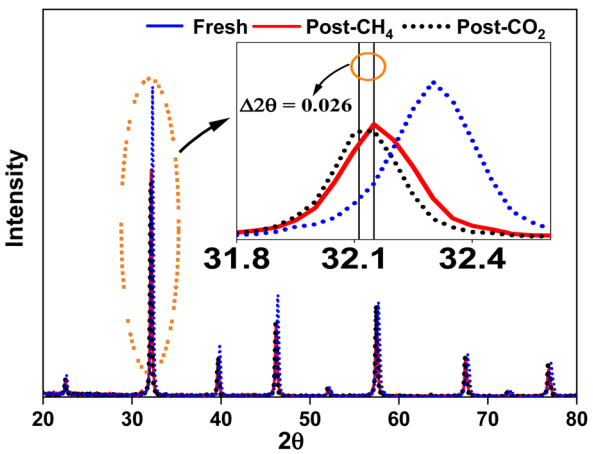

Fig. 6 XRD spectra of post-CH_4 and post-CO_2 Ru-LFM samples after 5 redox cycles.

3.4. Long-term stability test over Ru-LFM

Ru-LFM was exposed to 100 redox cycles to evaluate its long-term stability. The results of the redox experiments (Fig. 7) indicated that both CH_4 and CO_2 conversions were ≥85% up to cycle 30. However, ~25% performance loss was observed between the 31st and 100th cycles. Meanwhile, the H_2/CO ratio (Fig. S5†) and CO selectivity remained at ~2 and 95%, respectively. To reveal the reason for deactivation, XRD analysis of the post-100 cycles Ru-LFM sample was performed, which indicated the presence of a Mn_2O_3 phase (Fig. 8a). This suggests that there was some phase segregation that may have caused a slight deactivation. EDS mapping (Fig. 9) of the post-100 cycles Ru-LFM sample also confirmed such phase segregation.

Our recent study showed that the activity of a $LaNi_{0.5}Fe_{0.5}O_3$ based RC can be recovered with periodic air treatment,[20] which removes the deposited carbon. We attempted a similar strategy to reactivate the post-100 cycles Ru-LMF sample. Unlike $LaNi_{0.5}Fe_{0.5}O_3$, which was deactivated by carbon deposition, the product gas analysis from the packed bed during O_2-TPO indicated an oxygen uptake but with trace amounts of CO_x (Fig. 8b). This indicates that Ru-LFM was highly coke resistant and corroborated the 2 : 1 H_2/CO ratio we observed throughout the experiments. On the other hand, the XRD analysis of the fresh, post-100 cycles, and oxidized Ru-LFM samples in Fig. 8a indicated that the air oxidation step helped Mn_2O_3 to reincorporate into the mixed oxide phase, since no Mn_2O_3 peak was observed for the post-oxidation sample. Meanwhile, EDS mapping (Fig. S6†) of the post-O_2 TPO sample indicated that the distribution of metals (Fe, Mn, and La), although being more homogeneous than the post-100 cycles sample, still exhibited some degree of segregation. To confirm the effectiveness of air treatment in redistributing the segre-

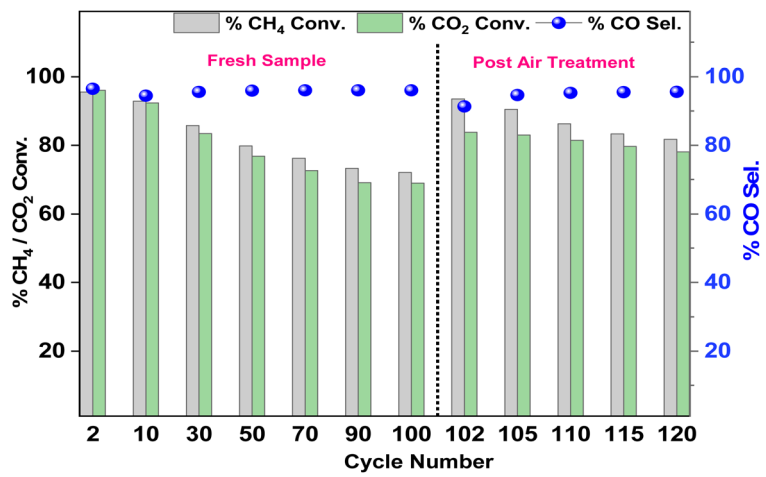

Fig. 7 CH_4/CO_2 conversions and CO selectivity for long-term tests with Ru-LFM.

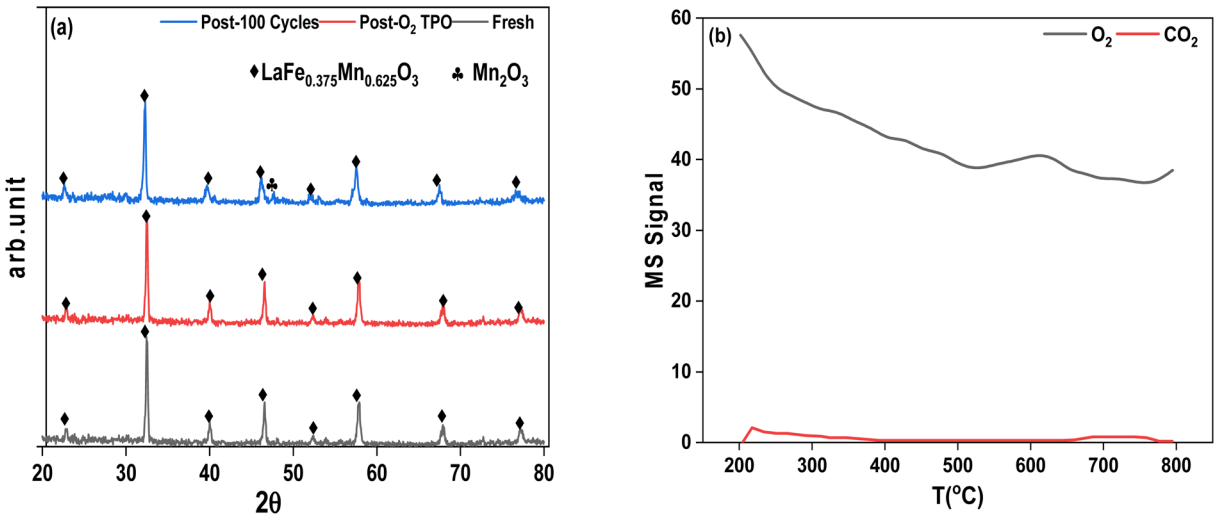

Fig. 8 (a) XRD spectra of fresh, post-100 cycles, and post-O_2 TPO Ru-LFM samples and (b) gas profiles during O_2-TPO.

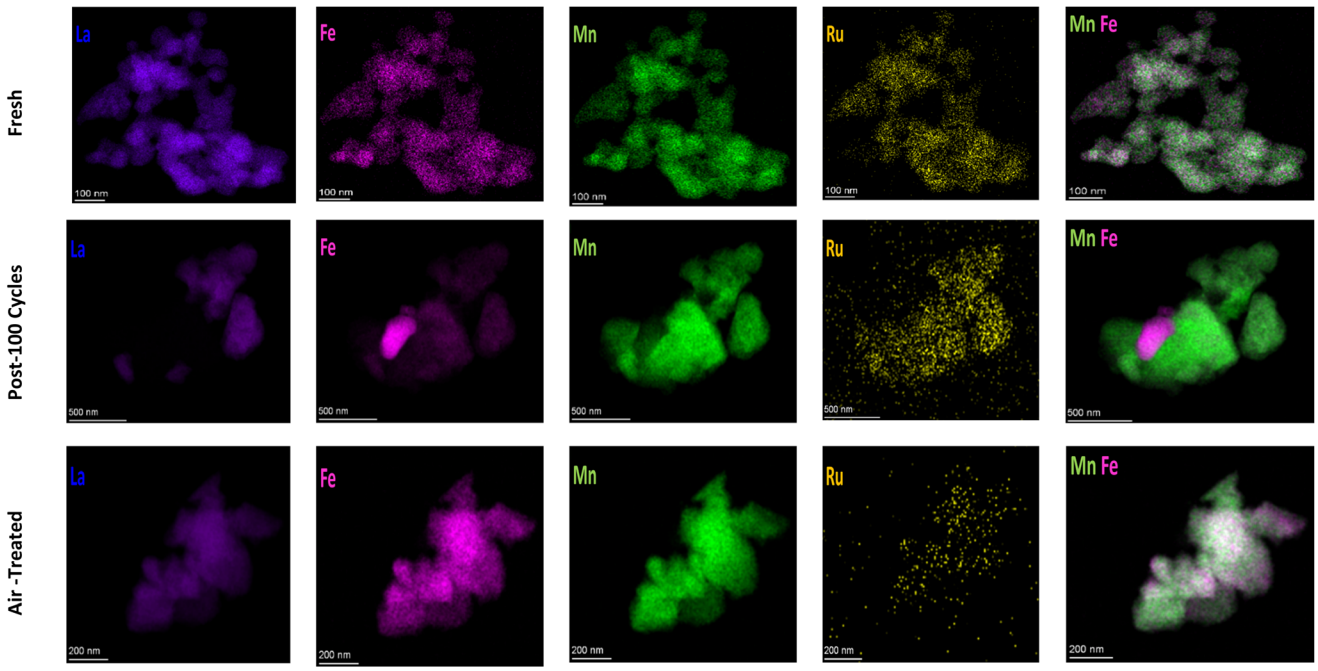

Fig. 9 EDS mappings of fresh, post-100 cycles, and air-treated Ru-LFM samples.

gated Mn, we further oxidized the post-100 cycles sample in the air for 60 minutes at 900 °C. EDS mapping of the air-treated sample (Fig. 9) indicated that the longer treatment with air was effective in promoting the homogeneous distribution of the cations, thereby restoring the initial activity of Ru-LFM. To further clarify, 20 additional cycles were performed. As can be seen from Fig. 7, the redox performance of the air-treated sample improved significantly where CH_4 and CO_2 conversions were ≥80% for the 20 additional cycles. This indicates that deep oxidation in air is an effective approach to reverse the deactivation of the redox catalyst. XPS analysis was also performed on the Ru-LFM samples (Fig. 10). Compared to the as-prepared sample, the post-100 cycles sample exhibited peak shifts of ~0.42 eV for Mn $2p_{3/2}$ and ~1.29 eV for Fe $2p_{3/2}$, both of which were towards the lower binding energy. After exposing the fresh redox catalyst to CH_4, the average oxidation state of the near-surface Fe decreased from approximately +3.4 to +2.1 and the oxidation state of Mn decreased from +3.3 to +2.6, based on peak fitting. After ending 100 cycles in the CO_2 step, the oxidation state of Fe was around +2.5 and Mn was approximately +2.7. In addition, both Mn^{4+} and Fe^{4+} shown in the fresh catalyst were not observed in the post-100 cycles sample.

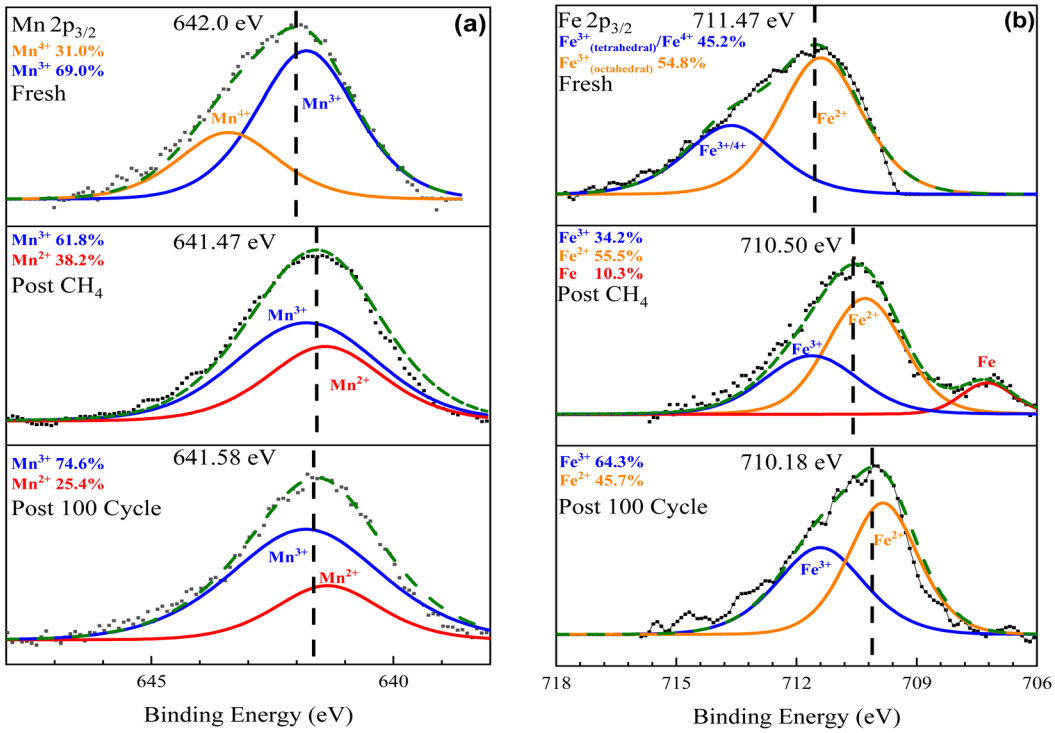

Fig. 10 XPS analysis of fresh, post-CH_4, and post-100 cycles Ru-LFM samples: (a) manganese[68–70] and (b) iron.[71–75]

These observations indicated that the perovskite structure was not fully re-oxidized under the CO_2 environment in the oxidation step. This is consistent with the DFT calculations, which indicated that the perovskite oxides would operate under certain oxygen vacancy ranges. The oxidation state changes for the near-surface B-site cations also correspond well to the redox reactions performed under HRP. Meanwhile, extended operation under oxygen-deficient conditions may have led to the phase segregation of Mn_2O_3. The XPS results also corroborate the earlier finding in a way that the air treatment would likely reactivate the catalyst because air would re-oxidize both Fe and Mn to higher oxidation states than CO_2 re-oxidation alone. This would promote the formation of the original LFM phase by reincorporating the segregated Mn_2O_3.

It is noted that the redox experiments were conducted within a temperature range of 800–950 °C. This temperature range is comparable to typical methane catalytic reforming conditions. The high CO_2 conversions, 85–100% for some of the RCs such as Ru-LFM reported in this study, compares favourably with other recent studies, such as membrane-based electroreduction, photoreduction and, thermochemical CO_2 conversion to CO[76,77] as well as the typical CO_2 splitting methods, such as thermochemical CO_2 splitting and dry reforming of methane.[25,48]

4. Conclusion

In this study, perovskite-structured redox catalysts (RCs) with the general formula $A_xA'_{1-x}B_yB'_{1-y}O_{3-\delta}$ (A/A′ = Sr, La, Y, Sm, Y; B/B′ = Fe, Mn, Ti) were investigated for CO_2-splitting and methane partial oxidation (POx) in a hybrid redox scheme. The specific oxide compositions, *i.e.*, $Sr_{0.625}La_{0.375}Fe_{0.625}Ti_{0.375}O_{3-\delta}$ (SLFT), $Sr_{0.5}Sm_{0.5}Fe_{0.625}Ti_{0.375}O_{3-\delta}$ (SSFT), $Sr_{0.625}Y_{0.375}Fe_{0.5}Ti_{0.5}O_{3-\delta}$ (SYFT), and $LaFe_{0.375}Mn_{0.625}O_{3-\delta}$ (LFM), were selected on DFT-based materials screening, which identified perovskite oxides with optimal equilibrium oxygen partial pressures (P_{O_2}s) for CO_2-splitting and methane partial oxidation. The experimental investigations confirmed the redox properties of the RCs for the proposed reactions. In addition, impregnation of the RCs with 1 wt% Ru was found to be highly effective in enhancing the reaction kinetics without altering the intrinsic redox thermodynamics of the oxide materials. For instance, impregnating 1 wt% Ru in LFM decreased the activation energies for the CH_4-POx and CO_2-splitting reactions by ~73% and 62%, respectively, when compared to the as-prepared LFM. XRD and TEM analysis indicated uniform elemental distribution for the as-prepared LFM and satisfactory Ru dispersion on the surface. Long-term redox testing over Ru-LFM indicated a stable performance for 30 cycles, followed by a ~25% decrease in the activity between the 31st and 100th cycles. Further characterization indicated that their deactivation resulted from the segregation of Mn, in the form of Mn_2O_3, from the LFM perovskite phase. Air treatment was shown to effectively promote the reincorporation of Mn into the perovskite phase, thereby reversing the deactivation of the redox catalyst. The DFT-guided mixed oxide design strategy, which was experimentally validated in this study, can be highly effective in further optimization of the redox catalysts

for CO_2 utilization. This study also reports effective approaches to enhance redox kinetics and long-term redox catalyst performance.

Author contributions

Sherafghan Iftikhar: methodology, redox catalyst synthesis, data collection and analysis, and writing – original draft and revision; William Martin: catalyst synthesis and data collection and analysis; Xijun Wang: DFT calculations and data analysis; Junchen Liu: data collection and analysis; Yunfei Gao: data analysis; Fanxing Li: supervision, conceptualization, methodology, and writing – revision and editing.

Conflicts of interest

There are no conflicts to declare.

Acknowledgements

This work was supported by the National Science Foundation (CBET – 1923468), the U.S. Department of Energy (Award DE-FE0031703), and the North Carolina State University Kenan Institute for Engineering, Technology and Science. The characterization work was performed in part at the Duke University Shared Materials Instrumentation Facility (SMIF). It was also performed in part at the Analytical Instrumentation Facility (AIF) at North Carolina State University, which is supported by the State of North Carolina and the National Science Foundation (award number ECCS-2025064). Both the SMIF and AIF are members of the North Carolina Research Triangle Nanotechnology Network (RTNN), a site in the National Nanotechnology Coordinated Infrastructure (NNCI).

References

1 R. G. Newell, D. Raimi and G. Aldana, Global Energy Outlook 2019: The Next Generation of, *Energy*, 2019, p. 46.
2 H.-J. Ho, A. Iizuka and E. Shibata, Carbon Capture and Utilization Technology without Carbon Dioxide Purification and Pressurization: A Review on Its Necessity and Available Technologies, *Ind. Eng. Chem. Res.*, 2019, **58**(21), 8941–8954, DOI: **10.1021/acs.iecr.9b01213**.
3 A. Mukherjee, J. A. Okolie, A. Abdelrasoul, C. Niu and A. K. Dalai, Review of Post-Combustion Carbon Dioxide Capture Technologies Using Activated Carbon, *J. Environ. Sci.*, 2019, **83**, 46–63, DOI: **10.1016/j.jes.2019.03.014**.
4 C. Du, P. Lu and N. Tsubaki, Efficient and New Production Methods of Chemicals and Liquid Fuels by Carbon Monoxide Hydrogenation, *ACS Omega*, 2020, **5**(1), 49–56, DOI: **10.1021/acsomega.9b03577**.
5 C. Mesters, A Selection of Recent Advances in C1 Chemistry, *Annu. Rev. Chem. Biomol. Eng.*, 2016, **7**(1), 223–238, DOI: **10.1146/annurev-chembioeng-080615-034616**.
6 S. C. Peter, Reduction of CO_2 to Chemicals and Fuels: A Solution to Global Warming and Energy Crisis, *ACS Energy Lett.*, 2018, **3**(7), 1557–1561, DOI: **10.1021/acsenergylett.8b00878**.
7 Z. Sun, T. Ma, H. Tao, Q. Fan and B. Han, Fundamentals and Challenges of Electrochemical CO_2 Reduction Using Two-Dimensional Materials, *Chem*, 2017, **3**(4), 560–587, DOI: **10.1016/j.chempr.2017.09.009**.
8 S. Xu and E. A. Carter, Theoretical Insights into Heterogeneous (Photo)Electrochemical CO_2 Reduction, *Chem. Rev.*, 2019, **119**(11), 6631–6669, DOI: **10.1021/acs.chemrev.8b00481**.
9 J. Wu, Y. Huang, W. Ye and Y. Li, CO_2 Reduction: From the Electrochemical to Photochemical Approach, *Adv. Sci.*, 2017, **4**(11), 1700194, DOI: **10.1002/advs.201700194**.
10 W. C. Chueh, C. Falter, M. Abbott, D. Scipio, P. Furler, S. M. Haile and A. Steinfeld, High-Flux Solar-Driven Thermochemical Dissociation of CO_2 and H_2O Using Nonstoichiometric Ceria, *Science*, 2010, **330**(6012), 1797–1801, DOI: **10.1126/science.1197834**.
11 A. J. Carrillo, A. H. Bork, T. Moser, E. Sediva, Z. D. Hood and J. L. M. Rupp, Modifying $La_{0.6}Sr_{0.4}MnO_3$ Perovskites with Cr Incorporation for Fast Isothermal CO_2 – Splitting Kinetics in Solar – Driven Thermochemical Cycles, *Adv. Energy Mater.*, 2019, **9**(28), 1803886, DOI: **10.1002/aenm.201803886**.
12 Y. Lu, L. Zhu, C. Agrafiotis, J. Vieten, M. Roeb and C. Sattler, Solar Fuels Production: Two-Step Thermochemical Cycles with Cerium-Based Oxides, *Prog. Energy Combust. Sci.*, 2019, **75**, 100785, DOI: **10.1016/j.pecs.2019.100785**.
13 M. Hoes, C. L. Muhich, R. Jacot, G. R. Patzke and A. Steinfeld, Thermodynamics of Paired Charge-Compensating Doped Ceria with Superior Redox Performance for Solar Thermochemical Splitting of H_2O and CO_2, *J. Mater. Chem. A*, 2017, **5**(36), 19476–19484, DOI: **10.1039/C7TA05824A**.
14 C. Muhich, M. Hoes and A. Steinfeld, Mimicking Tetravalent Dopant Behavior Using Paired Charge Compensating Dopants to Improve the Redox Performance of Ceria for Thermochemically Splitting H_2O and CO_2, *Acta Mater.*, 2018, **144**, 728–737, DOI: **10.1016/j.actamat.2017.11.022**.
15 A. J. Carrillo, K. J. Kim, Z. D. Hood, A. H. Bork and J. L. M. Rupp, $La_{0.6}Sr_{0.4}Cr_{0.8}Co_{0.2}O_3$ Perovskite Decorated with Exsolved Co Nanoparticles for Stable CO_2 Splitting and Syngas Production, *ACS Appl. Energy Mater.*, 2020, **3**(5), 4569–4579, DOI: **10.1021/acsaem.0c00249**.
16 S. Ackermann, L. Sauvin, R. Castiglioni, J. L. M. Rupp, J. R. Scheffe and A. Steinfeld, Kinetics of CO_2 Reduction over Nonstoichiometric Ceria, *J. Phys. Chem. C*, 2015, **119**(29), 16452–16461, DOI: **10.1021/acs.jpcc.5b03464**.
17 L. J. Venstrom, R. M. De Smith, Y. Hao, S. M. Haile and J. H. Davidson, Efficient Splitting of CO 2 in an Isothermal

Redox Cycle Based on Ceria, *Energy Fuels*, 2014, **28**(4), 2732–2742, DOI: **10.1021/ef402492e**.

18 I. Al-Shankiti, B. D. Ehrhart and A. W. Weimer, Isothermal Redox for H_2O and CO_2 Splitting – A Review and Perspective, *Sol. Energy*, 2017, **156**, 21–29, DOI: **10.1016/j.solener.2017.05.028**.

19 S. Iftikhar, W. Martin, Y. Gao, X. Yu, I. Wang, Z. Wu and F. Li, $LaNi_xFe_{1-x}O_3$ as Flexible Oxygen or Carbon Carriers for Tunable Syngas Production and CO_2 Utilization, *Catal. Today*, 2022, S0920586122003029, DOI: **10.1016/j.cattod.2022.07.022**.

20 S. Iftikhar, Q. Jiang, Y. Gao, J. Liu, H. Gu, L. Neal and F. Li, $LaNi_x,Fe_{1-x}O_{3-\delta}$ as a Robust Redox Catalyst for CO_2 Splitting and Methane Partial Oxidation, *Energy Fuels*, 2021, **35**(17), 13921–13929, DOI: **10.1021/acs.energyfuels.1c02258**.

21 Q. Jiang, Y. Gao, V. P. Haribal, H. Qi, X. Liu, H. Hong, H. Jin and F. Li, Mixed Conductive Composites for 'Low-Temperature' Thermo-Chemical CO_2 Splitting and Syngas Generation, *J. Mater. Chem. A*, 2020, **8**(26), 13173–13182, DOI: **10.1039/D0TA03232H**.

22 J. Zhang, V. Haribal and F. Li, Perovskite Nanocomposites as Effective CO_2-Splitting Agents in a Cyclic Redox Scheme, *Sci. Adv.*, 2017, **3**(8), e1701184, DOI: **10.1126/sciadv.1701184**.

23 V. P. Haribal, X. Wang, R. Dudek, C. Paulus, B. Turk, R. Gupta and F. Li, Modified Ceria for "Low-Temperature" CO_2 Utilization: A Chemical Looping Route to Exploit Industrial Waste Heat, *Adv. Energy Mater.*, 2019, **9**(41), 1901963, DOI: **10.1002/aenm.201901963**.

24 X. Wang, Y. Gao, E. Krzystowczyk, S. Iftikhar, J. Dou, R. Cai, H. Wang, C. Ruan, S. Ye and F. Li, High-Throughput Oxygen Chemical Potential Engineering of Perovskite Oxides for Chemical Looping Applications, *Energy Environ. Sci.*, 2022, **15**(4), 1512–1528, DOI: **10.1039/D1EE02889H**.

25 S. Bhavsar, M. Najera and G. Veser, Chemical Looping Dry Reforming as Novel, Intensified Process for CO_2 Activation, *Chem. Eng. Technol.*, 2012, **35**(7), 1281–1290, DOI: **10.1002/ceat.201100649**.

26 B. Bulfin, S. Ackermann, P. Furler and A. Steinfeld, Thermodynamic Comparison of Solar Methane Reforming via Catalytic and Redox Cycle Routes, *Sol. Energy*, 2021, **215**, 169–178, DOI: **10.1016/j.solener.2020.11.076**.

27 R. Peng, Y. Chen, B. Zhang, Z. Li, X. Cui, C. Guo, Y. Zhao and J. Zhang, Tailoring the Stability of Ni-Fe/Mayenite in Methane – Carbon Dioxide Reforming, *Fuel*, 2021, **284**, 118909, DOI: **10.1016/j.fuel.2020.118909**.

28 I. Wang, Y. Gao, X. Wang, R. Cai, C. Chung, S. Iftikhar, W. Wang and F. Li, Liquid Metal Shell as an Effective Iron Oxide Modifier for Redox-Based Hydrogen Production at Intermediate Temperatures, *ACS Catal.*, 2021, **11**(16), 10228–10238, DOI: **10.1021/acscatal.1c02102**.

29 W. Liu, Controlling Lattice Oxygen Activity of Oxygen Carrier Materials by Design: A Review and Perspective, *React. Chem. Eng.*, 2021, **6**(9), 1527–1537, DOI: **10.1039/D1RE00209K**.

30 J. Adanez, A. Abad, F. Garcia-Labiano, P. Gayan and L. F. de Diego, Progress in Chemical-Looping Combustion and Reforming Technologies, *Prog. Energy Combust. Sci.*, 2012, **38**(2), 215–282, DOI: **10.1016/j.pecs.2011.09.001**.

31 X. Zhu, Q. Imtiaz, F. Donat, C. R. Müller and F. Li, Chemical Looping beyond Combustion – a Perspective, *Energy Environ. Sci.*, 2020, **13**(3), 772–804, DOI: **10.1039/C9EE03793D**.

32 L.-S. Fan, L. Zeng, W. Wang and S. Luo, Chemical Looping Processes for CO_2 Capture and Carbonaceous Fuel Conversion – Prospect and Opportunity, *Energy Environ. Sci.*, 2012, **5**(6), 7254, DOI: **10.1039/c2ee03198a**.

33 L. Zeng, Z. Cheng, J. A. Fan, L.-S. Fan and J. Gong, Metal Oxide Redox Chemistry for Chemical Looping Processes, *Nat. Rev. Chem.*, 2018, **2**(11), 349–364, DOI: **10.1038/s41570-018-0046-2**.

34 V. V. Galvita, H. Poelman, V. Bliznuk, C. Detavernier and G. B. Marin, CeO_2-Modified Fe_2O_3 for CO_2 Utilization via Chemical Looping, *Ind. Eng. Chem. Res.*, 2013, **52**(25), 8416–8426, DOI: **10.1021/ie4003574**.

35 V. V. Galvita, H. Poelman, C. Detavernier and G. B. Marin, Catalyst-Assisted Chemical Looping for CO_2 Conversion to CO, *Appl. Catal., B*, 2015, **164**, 184–191, DOI: **10.1016/j.apcatb.2014.09.007**.

36 A. Fossdal, M.-A. Einarsrud and T. Grande, Phase Equilibria in the Pseudo-Binary System SrO–Fe_2O_3, *J. Solid State Chem.*, 2004, **177**(8), 2933–2942, DOI: **10.1016/j.jssc.2004.05.007**.

37 L. M. Neal, A. Shafiefarhood and F. Li, Dynamic Methane Partial Oxidation Using a Fe_2O_3@$La_{0.8}Sr_{0.2}FeO_{3-\delta}$ Core–Shell Redox Catalyst in the Absence of Gaseous Oxygen, *ACS Catal.*, 2014, **4**(10), 3560–3569, DOI: **10.1021/cs5008415**.

38 F. He, J. Trainham, G. Parsons, J. S. Newman and F. Li, A Hybrid Solar-Redox Scheme for Liquid Fuel and Hydrogen Coproduction, *Energy Environ. Sci.*, 2014, **7**(6), 2033–2042, DOI: **10.1039/C4EE00038B**.

39 F. He and F. Li, Perovskite Promoted Iron Oxide for Hybrid Water-Splitting and Syngas Generation with Exceptional Conversion, *Energy Environ. Sci.*, 2015, **8**(2), 535–539, DOI: **10.1039/C4EE03431G**.

40 F. R. García-García and I. S. Metcalfe, Chemical Looping Dry Reforming of Methane Using Mixed Oxides of Iron and Cerium: Operation Window, *Catal. Commun.*, 2021, **160**, 106356, DOI: **10.1016/j.catcom.2021.106356**.

41 D. Kang, H. S. Lim, M. Lee and J. W. Lee, Syngas Production on a Ni-Enhanced Fe_2O_3/Al_2O_3 Oxygen Carrier via Chemical Looping Partial Oxidation with Dry Reforming of Methane, *Appl. Energy*, 2018, **211**, 174–186, DOI: **10.1016/j.apenergy.2017.11.018**.

42 J. Guerrero-Caballero, T. Kane, N. Haidar, L. Jalowiecki-Duhamel and A. Löfberg, Ni, Co, Fe Supported on Ceria and Zr Doped Ceria as Oxygen Carriers for Chemical Looping Dry Reforming of Methane, *Catal. Today*, 2019, **333**, 251–258, DOI: **10.1016/j.cattod.2018.11.064**.

43 A. More, S. Bhavsar and G. Veser, Iron–Nickel Alloys for Carbon Dioxide Activation by Chemical Looping Dry

Reforming of Methane, *Energy Technol.*, 2016, **4**(10), 1147–1157, DOI: 10.1002/ente.201500539.

44 J.-M. Lavoie, Review on Dry Reforming of Methane, a Potentially More Environmentally-Friendly Approach to the Increasing Natural Gas Exploitation, *Front. Chem.*, 2014, **2**, 1–17, DOI: 10.3389/fchem.2014.00081.

45 A. Löfberg, J. Guerrero-Caballero, T. Kane, A. Rubbens and L. Jalowiecki-Duhamel, Ni/CeO_2 Based Catalysts as Oxygen Vectors for the Chemical Looping Dry Reforming of Methane for Syngas Production, *Appl. Catal., B*, 2017, **212**, 159–174, DOI: 10.1016/j.apcatb.2017.04.048.

46 H. Gu, Y. Gao, S. Iftikhar and F. Li, Ce Stabilized Ni–SrO as a Catalytic Phase Transition Sorbent for Integrated CO_2 Capture and CH_4 Reforming, *J. Mater. Chem. A*, 2022, **10**(6), 3077–3085, DOI: 10.1039/D1TA09967A.

47 S. Bhavsar and G. Veser, Chemical Looping beyond Combustion: Production of Synthesis Gas via Chemical Looping Partial Oxidation of Methane, *RSC Adv.*, 2014, **4**(88), 47254–47267, DOI: 10.1039/C4RA06437B.

48 M. Najera, R. Solunke, T. Gardner and G. Veser, Carbon Capture and Utilization via Chemical Looping Dry Reforming, *Chem. Eng. Res. Des.*, 2011, **89**(9), 1533–1543, DOI: 10.1016/j.cherd.2010.12.017.

49 S. Bhavsar, M. Najera, R. Solunke and G. Veser, Chemical Looping: To Combustion and Beyond, *Catal. Today*, 2014, **228**, 96–105, DOI: 10.1016/j.cattod.2013.12.025.

50 Y. Zheng, K. Li, H. Wang, D. Tian, Y. Wang, X. Zhu, Y. Wei, M. Zheng and Y. Luo, Designed Oxygen Carriers from Macroporous $LaFeO_3$ Supported CeO_2 for Chemical-Looping Reforming of Methane, *Appl. Catal., B*, 2017, **202**, 51–63, DOI: 10.1016/j.apcatb.2016.08.024.

51 K. Li, H. Wang and Y. Wei, Syngas Generation from Methane Using a Chemical-Looping Concept: A Review of Oxygen Carriers, *J. Chem.*, 2013, 1–8, DOI: 10.1155/2013/294817.

52 Y. Zhu, W. Liu, X. Sun, X. Ma, Y. Kang, X. Wang and J. Wang, La-Hexaaluminate for Synthesis Gas Generation by Chemical Looping Partial Oxidation of Methane Using CO_2 as Sole Oxidant, *AIChE J.*, 2018, **64**(2), 550–563, DOI: 10.1002/aic.15942.

53 Y. Zhu, R. Liu, X. Sun, X. Ma, X. Wang and H. Tian, Metal Modified Hexaaluminates for Syngas Generation and CO_2 Utilization via Chemical Looping, *Int. J. Hydrogen Energy*, 2019, **44**(21), 10218–10231, DOI: 10.1016/j.ijhydene.2019.02.187.

54 J. Hu, S. Chen and W. Xiang, Ni, Co and Cu-Promoted Iron-Based Oxygen Carriers in Methane-Fueled Chemical Looping Hydrogen Generation Process, *Fuel Process. Technol.*, 2021, **221**, 106917, DOI: 10.1016/j.fuproc.2021.106917.

55 V. P. Haribal, F. He, A. Mishra and F. Li, Iron-Doped $BaMnO_3$ for Hybrid Water Splitting and Syngas Generation, *ChemSusChem*, 2017, **10**(17), 3402–3408, DOI: 10.1002/cssc.201700699.

56 M. Tang, L. Xu and M. Fan, Progress in Oxygen Carrier Development of Methane-Based Chemical-Looping Reforming: A Review, *Appl. Energy*, 2015, **151**, 143–156, DOI: 10.1016/j.apenergy.2015.04.017.

57 Z. Miao, Z. Hu, E. Jiang and X. Ma, Hydrogen-Rich Syngas Production by Chemical Looping Reforming on Crude Wood Vinegar Using Ni-Modified HY Zeolite Oxygen Carrier, *Fuel*, 2020, **279**, 118547, DOI: 10.1016/j.fuel.2020.118547.

58 N. Galinsky, M. Sendi, L. Bowers and F. Li, $CaMn_{1-B}O_3$– (B = Al, V, Fe, Co, and Ni) Perovskite Based Oxygen Carriers for Chemical Looping with Oxygen Uncoupling (CLOU), *Appl. Energy*, 2016, **174**, 80–87, DOI: 10.1016/j.apenergy.2016.04.046.

59 Y. Long, Z. Gu, S. Lin, K. Yang, X. Zhu, Y. Wei, H. Wang and K. Li, NiO and CuO Coated Monolithic Oxygen Carriers for Chemical Looping Combustion of Methane, *J. Energy Inst.*, 2021, **94**, 199–209, DOI: 10.1016/j.joei.2020.09.004.

60 S. Bhattar, M. A. Abedin, S. Kanitkar and J. J. Spivey, A Review on Dry Reforming of Methane over Perovskite Derived Catalysts, *Catal. Today*, 2021, **365**, 2–23, DOI: 10.1016/j.cattod.2020.10.041.

61 A. M. Deml, V. Stevanović, A. M. Holder, M. Sanders, R. O'Hayre and C. B. Musgrave, Tunable Oxygen Vacancy Formation Energetics in the Complex Perovskite Oxide Sr_x, $La_{1-x}Mn_yAl_{1-y}O_3$, *Chem. Mater.*, 2014, **26**(22), 6595–6602, DOI: 10.1021/cm5033755.

62 T. O. L. Sunde, T. Grande and M.-A. Einarsrud, *Modified Pechini Synthesis of Oxide Powders and Thin Films*, 2016, p. 21.

63 K. Zhang, R. Ran, L. Ge, Z. Shao, W. Jin and N. Xu, Double-Site Yttria-Doped $Sr_{1-x}Y_xCo_{1-y}Y_yO_{3-\delta}$ Perovskite Oxides as Oxygen Semi-Permeable Membranes, *J. Alloys Compd.*, 2009, **474**(1–2), 477–483, DOI: 10.1016/j.jallcom.2008.06.120.

64 I. Luisetto, C. Sarno, D. De Felicis, F. Basoli, C. Battocchio, S. Tuti, S. Licoccia and E. Di Bartolomeo, Ni Supported on γ-Al 2 O 3 Promoted by Ru for the Dry Reforming of Methane in Packed and Monolithic Reactors, *Fuel Process. Technol.*, 2017, **158**, 130–140, DOI: 10.1016/j.fuproc.2016.12.015.

65 K. Nagaoka, M. Okamura and K. Aika, Titania Supported Ruthenium as a Coking-Resistant Catalyst for High Pressure Dry Reforming of Methane, *Catal. Commun.*, 2001, **2**(8), 255–260, DOI: 10.1016/S1566-7367(01)00043-7.

66 P. Ferreira-Aparicio, I. Rodríguez-Ramos, J. A. Anderson and A. Guerrero-Ruiz, Mechanistic Aspects of the Dry Reforming of Methane over Ruthenium Catalysts, *Appl. Catal., A*, 2000, **202**(2), 183–196, DOI: 10.1016/S0926-860X(00)00525-1.

67 R. L. Blaine and H. E. Kissinger, Homer Kissinger and the Kissinger Equation, *Thermochim. Acta*, 2012, **540**, 1–6, DOI: 10.1016/j.tca.2012.04.008.

68 V. Di Castro and G. Polzonetti, XPS Study of MnO Oxidation, *J. Electron Spectrosc. Relat. Phenom.*, 1989, **48**(1), 117–123, DOI: 10.1016/0368-2048(89)80009-X.

69 Y. Umezawa and C. N. Reilley, Effect of Argon Ion Bombardment on Metal Complexes and Oxides Studied by

X-Ray Photoelectron Spectroscopy, *Anal. Chem.*, 1978, **50**(9), 1290–1295, DOI: **10.1021/ac50031a025**.

70 B. R. Strohmeier and D. M. Hercules, Surface Spectroscopic Characterization of Manganese/Aluminum Oxide Catalysts, *J. Phys. Chem.*, 1984, **88**(21), 4922–4929, DOI: **10.1021/j150665a026**.

71 P. Mills and J. L. Sullivan, A Study of the Core Level Electrons in Iron and Its Three Oxides by Means of X-Ray Photoelectron Spectroscopy, *J. Phys. D: Appl. Phys.*, 1983, **16**(5), 723–732, DOI: **10.1088/0022-3727/16/5/005**.

72 R. G. C. Moore, S. D. Evans, T. Shen and C. E. C. Hodson, Room-Temperature Single-Electron Tunnelling in Surfactant Stabilised Iron Oxide Nanoparticles, *Phys. E*, 2001, **9**(2), 253–261, DOI: **10.1016/S1386-9477(00)00279-4**.

73 D. D. Hawn and B. M. DeKoven, Deconvolution as a Correction for Photoelectron Inelastic Energy Losses in the Core Level XPS Spectra of Iron Oxides, *Surf. Interface Anal.*, 1987, **10**(2–3), 63–74, DOI: **10.1002/sia.740100203**.

74 X. Zhao, Q. Yang and J. Cui, XPS Study of Surface Absorbed Oxygen of ABO_3 Mixed Oxides, *J. Rare Earths*, 2008, **26**(4), 511–514, DOI: **10.1016/S1002-0721(08)60128-3**.

75 S. Poulin, R. França, L. Moreau-Bélanger and E. Sacher, Confirmation of X-Ray Photoelectron Spectroscopy Peak Attributions of Nanoparticulate Iron Oxides, Using Symmetric Peak Component Line Shapes, *J. Phys. Chem. C*, 2010, **114**(24), 10711–10718, DOI: **10.1021/jp100964x**.

76 Y. Guo, C. Qian, Y. Wu, J. Liu, X. Zhang, D. Wang and Y. Zhao, Porous Catalytic Membranes for CO_2 Conversion, *J. Energy Chem.*, 2021, **63**, 74–86, DOI: **10.1016/j.jechem.2021.06.008**.

77 K. Feng, Y. Wang, M. Guo, J. Zhang, Z. Li, T. Deng, Z. Zhang and B. Yan, *In situ*/Operando Techniques to Identify Active Sites for Thermochemical Conversion of CO_2 over Heterogeneous Catalysts, *J. Energy Chem.*, 2021, **62**, 153–171, DOI: **10.1016/j.jechem.2021.03.054**.